Plasma Sources Science and Technology

The attachment length in orificed hollow cathodes

To cite this article before publication: Christopher Wordingham *et al* 2021 *Plasma Sources Sci. Technol.* in press https://doi.org/10.1088/1361-6595/ac3d3f

The Attachment Length in Orificed Hollow Cathodes

C J Wordingham, P-Y C R Taunay, and E Y Choueiri

Electric Propulsion and Plasma Dynamics Laboratory, Princeton University, Princeton, NJ 08544, USA

E-mail: cjw4@alumni.princeton.edu,ptaunay@princeton.edu

Abstract.

A first-principles approach to obtain the attachment length within a hollow cathode with a constrictive orifice, and its scaling with internal cathode pressure, is developed. This parameter, defined herein as the plasma density decay length scale upstream of (away from) the cathode orifice, is critical because it controls the utilization of the hollow cathode insert and influences cathode life. A two-dimensional framework is developed from the ambipolar diffusion equation for the insert-region plasma. A closed-form solution for the plasma density is obtained using standard partial differential equation techniques by applying an approximate boundary condition at the cathode orifice plane. This approach also yields the attachment length and electron temperature without reliance on measured plasma property data or complex computational models. The predicted plasma density profile is validated against measurements from the NSTAR discharge cathode, and calculated electron temperatures and attachment lengths agree with published values. Nondimensionalization of the governing equations reveals that the solution depends almost exclusively on the neutral pressure-diameter product in the insert plasma region. Evaluation of analytical results over a wide range of input parameters yields scaling relations for the variation of the attachment length and electron temperature with the pressure-diameter product. For the range of orifice-to-insert diameter ratio studied, the influence of orifice size is shown to be small except through its effect on insert pressure, and the attachment length is shown to be proportional to the insert inner radius, suggesting high-pressure cathodes should be constructed with larger-diameter inserts.

Keywords: hollow cathode, thermionic, experimental validation, electric propulsion, plasma propulsion, low-temperature plasma

Submitted to: *Plasma Sources Sci. Technol.*

1. Introduction

Hollow cathodes are critical components for a number of technologies and applications, including surface processing, [1–3] neutral-beam injection for fusion devices, [4–7] and plasma propulsion [8–29]. The reliable operation of these devices, however, is particularly important for in-space electric propulsion. In this application, hollow cathodes provide electron current for both plasma generation and beam neutralization and (except during ground testing) cannot be readily serviced or replaced. Orificed hollow cathodes for next-generation Hall and ion thrusters will require increasingly high discharge currents and operational lifetimes. "Near-term" projections for the required discharge powers are in the range of 100 to 200 kW, [30] with some proposed missions demanding operational lifetimes of up to 100 kh. [29, 31] For a specific impulse in the 2000 to 6000 s range, this translates to discharge currents of up to 700 A. [28, 32] Cathodes operating at lower current have undergone life tests of up to 50 kh. [26] Higher-current cathodes capable of providing up to 300 A of discharge current have been developed, [28,33] with estimated lifetimes of 10 to 20 kh for those developed by Goebel *et al.* [28] Because life tests are both time-consuming and costly, there is a clear need for the development of methods that can accurately predict the operational life of hollow cathodes. The lifetime of a cathode is limited by erosion of external surfaces (most notably the keeper electrode) and, fundamentally, by erosion or evaporation of emitter material. To estimate the evaporation rate of the emitter material we must estimate the area over which the discharge current is extracted, which depends on both the plasma density and emitter temperature profiles.

The length within a hollow cathode over which the internal plasma is sufficiently dense to support temperature-limited thermionic emission, or where plasma is "attached," not only influences the emitter temperature profile, but also its operational life and the maximum current that can be extracted before the emitter evaporation rate becomes too great. Emission current density inferred from measured insert temperature or plasma density profiles is typically axially nonuniform, and may peak sharply near the orifice (especially for high-pressure dispenser cathodes). [27,34] The axial plasma density maximum near the orifice creates the possibility for space-charge-limited emission in the upstream portion of the emitter. This makes prediction of the emitter life substantially more difficult than for vacuum cathodes.

The attachment length has been identified by several terms including: emission length [35], active zone [36], plasma penetration depth [35], conduction length [27], or ion production region [37]. These terms are often used interchangeably. However, it is not guaranteed that ion production prevents space-charge-limited emission (*i.e.*, the ion production region and attachment length may not coincide). In addition, plasma may not extend over the entire region of maximum emitter temperature, which typically characterizes the active zone. Early work on tube hollow cathodes (*i.e.*, with no orifice constriction) showed that the dense plasma may also extend *beyond* the active emission area [36]. The typical attachment length or "active zone" for a tube cathode is on the order of the tube diameter, and this region can occur upstream from the exit by approximately the tube diameter [22]. No simple relationship between the cathode geometry and attachment length has been published for orificed hollow cathodes. Increasing the pressure or discharge current also tends to decrease the attachment length within an orificed hollow cathode [27, 35]. If the pressure is reduced, the attachment length tends to increase, but usually at the cost of higher sheath voltages — and increased exposure to the collisionless plume plasma in the case of very large orifice diameters [27, 35] — increasing ion bombardment energies at the emitter surface. In early experiments with a mercury-fed orificed hollow cathode, Siegfried and Wilbur [21] found that the distribution of emission current density and insert temperatures (and therefore the attachment length) were insensitive to changes in orifice size or total discharge current when the internal pressure was held constant.

Several approaches to calculate the attachment length have been proposed. 0-D models either include a direct dependence of the attachment length on the energy-exchange mean free path for emitted electrons [18, 19], an ambipolar-diffusion-dominated density decay [27], empirical correlations of the attachment length with cathode internal pressure [35], iterative calculations minimizing power deposited in the sheath [24], or use the attachment length as a free parameter to fit experimental data [35]. Both the

empirical pressure correlation and the electron-energy-exchange mean free path approaches have drawbacks when applied to new or different cathodes than those for which they were originally developed. The latter approach, for instance, vastly underpredicts the length scale over which the plasma density decays when applied to the NSTAR discharge cathode, and the former tends to require parameters outside the range of proposed values to fit experimental data. [38] One- [39] and two-dimensional models [40–42] have typically required experimental data as input, usually in the form of the axial emitter temperature profile. One method to remove the dependence on experimental emitter temperature data is the use of a coupled plasma-thermal model, as described in [43–46]. However, coupled plasma-thermal models require detailed information about the thermal configuration of the cathode and its environment. Thermal property data (*e.g.*, conductivity and emissivity) of some cathode materials are also not well-characterized experimentally (*e.g.*, emissivity measurements [47, 48] of lanthanum hexaboride). In this work, we present an alternative and expedient analytical approach that does not rely on the cathode thermal configuration to obtain scaling of the attachment length.

We have chosen to revisit the ambipolar-diffusion-dominated density decay proposed by Goebel and Katz in [27], altering it to provide a self-consistent theoretical framework to estimate the attachment length while minimizing the dependence on experimental data. The model of [27] requires the on-axis plasma potential, total emitter heat loss, and total ion current (from measurements and/or a 2-D computational model anchored with experimental data) in order to predict the attachment length. [38] This renders the original model effectively semi-empirical in terms of capturing the attachment length.

A complete 2-D description of all plasma species (neutrals, ions, and electrons) such as proposed in [41–43, 49, 50] combined with a thermal model is beyond the scope of this work. Our approach also cannot be readily used for a detailed investigation of the effects of the thermal design of a given device on the attachment length. Our goal is not the detailed simulation of experiments, but rather understanding of the basic scaling and nature of physical mechanisms within hollow cathodes. To the authors' knowledge, no approximate formulae like those given in our work have been produced by 2-D modeling efforts in the open literature. For codes that do not depend on experimental data, studies similar to ours could yield further insight as 2-D codes can provide particle fluxes to the walls, insert density profiles, and emitter temperature profiles.

We solve a 0-D plasma power balance for the average orifice plasma density, the 1-D radial ambipolar diffusion equation for the electron temperature and plasma density profile in the orifice region, and the 2-D ambipolar diffusion equation for the electron temperature and plasma density profile within the insert region. The attachment length is deduced from the axial plasma density decay length scale in the insert region plasma. Our approach differs from that presented in [27] in that it considers appropriate boundary conditions for lower pressure cathodes, does not rely on experimental data as input, features a continuous plasma density profile between the orifice and insert regions, and uses a complete orthogonal basis to represent the solution of the ambipolar diffusion equation.

In Section 2 we discuss the overarching assumptions of our approach that are common to all regions. In Sections 3 and 4, we present the one- and two-dimensional approaches for the orifice and insert plasma regions, respectively. Governing equations are nondimensionalized and the controlling parameters are identified. We show a direct comparison of our solution to previous numerical results and experimental data in Section 5. We perform a sensitivity analysis as part of the plasma density profile validation. Finally, scaling relationships for the analytically obtained attachment length and electron temperature with cathode operating pressure are obtained from fits to the results of a parametric study.

2. Assumptions

The fundamental assumptions required for the analytical solution of the proposed approach are the following:

(i) The plasma density in the insert region is governed by resonant-charge-exchange-limited ambipolar diffusion (with the implicit assumption of quasineutrality).

(ii) The Bohm and ambipolar diffusion fluxes are equal at the plasma-sheath boundary, and the Bohm velocity does not depend on the emission current.

(iii) The neutral pressures and heavy particle temperatures are constant in each of the considered regions.

(iv) The electron temperature in each region is constant.

(v) The orifice plasma density is axially uniform.

(vi) The plasma density is continuous across the orifice/insert boundary and decays exponentially in the radial direction along the orifice plate.

(vii) The net ion flux across the plane parallel to the orifice plate surface in the insert region is zero.

Our first assumption is generally justified for the noble gases for which the cross section for resonant

charge exchange is very large [27, 51, 52] and the electron mobility is much larger than the ion mobility.

The second assumption allows for an improvement over previously considered boundary conditions (*e.g.*, those used in [27,39]) in that the plasma density is not assumed to be zero at the "wall" or, more accurately, the plasma-sheath boundary. This boundary condition is more general and is often applied in other areas of plasma physics. [53, 54] This boundary condition is obtained using ion continuity under the assumption that there is no ionization in the sheath (a reasonable assumption for the insert-region plasma within orificed hollow cathodes). Asserting that the plasma density vanishes at the boundary overestimates the diffusion losses to the walls and therefore overpredicts the required electron temperature for a given cathode pressure and geometry. Taking the sheath-edge ion velocity to be equal to the Bohm velocity greatly simplifies the dependence of the boundary conditions on operating conditions. This assumption has been used in many cathode models, including some 2-D computational models. [43] This approximation is also reasonable because the energy of ions entering the sheath does not typically vary by more than 20% of the value for a non-emitting wall. [55, 56]

Because we limit the study to the ambipolar diffusion region within the cathode, our approach is unable to determine the sheath potential or the emitter temperature directly. Those quantities, along with the bulk plasma density, would be necessary to evaluate the sputtering and evaporation rates of the emitter and determine its lifetime. While the plasma density obtained with our approach may be used to determine the plasma potential structure within the ambipolar region (*e.g.*, using current continuity [53]), proper sheath modeling on all cathode surfaces would still be required. This is beyond the scope of this work: the ambipolar diffusion framework we consider here is not applicable to the sheath region because it is not quasineutral and models only the ions for which the effects of the sheath voltage, surface emission, and current-carrying plasma are small or negligible.

Two-dimensional computational model predictions suggest that the assumption of constant heavy particle temperature in the orifice and insert regions may be challenged (see, *e.g.*, [43,57]). However, due to the lack of experimental data, it is difficult to determine how well we can approximate the neutral or ion temperatures as constants in either region. This assumption is nonetheless common to most approaches and is justified in a later section via sensitivity analysis. Assumption (iii) approximates the behavior of the insert-region total pressure for cathodes with orifices that are sufficiently constricted with respect to the insert diameter. For these cathodes, the Mach and Reynolds numbers are both low in the insert region; due to the relative size of the orifice, most of the pressure drop associated with the cathode flow should occur along the length of the orifice channel. The assumption of constant insert-region pressure (adopted in the approaches of [19,27,39,58]) has previously been justified by applying Poiseuille flow theory [27, 59]. Poiseuille flow models, however, are not strictly applicable to the cathode flow and fail to incorporate the two-dimensional effects near the orifice constriction. Strong pressure gradients are likely to exist in the orifice (and, possibly, in the near-orifice region), but we assume constant pressure in the orifice region and use the average pressure in order to make the solution tractable. The assumption that the orifice plasma density is axially uniform is likely to be equally unjustified. It is equivalent to averaging the 2-D orifice computational region over a single direction. These assumptions represent potential limitations of our approach, but we have chosen to restrict our focus to the density decay in the insert region. We therefore use a one-dimensional radial diffusion representation of the orifice plasma to capture the effect of the orifice size and radial density distribution without making the solution exceedingly complex.

Our final two assumptions are unique to our approach and are used to couple the insert and orifice solutions and to calculate the insert electron temperature, respectively. The last assumption implies that the maximum radially averaged plasma density occurs at the orifice inlet surface and approximates the behavior of the plasma density for cathodes with constricted orifices operated at relatively high pressure, for which the plasma density peak occurs near the orifice. Imposing the Bohm flux along the orifice plate surface and a separate flux across the orifice inlet surface might prove to be a more physically accurate constraint, but cannot be implemented without knowledge of the ion flux across the orifice inlet.

As opposed to modern 2-D computational codes, our approach is therefore not able to capture the near-orifice density variation for cathodes in which the peak occurs upstream of the orifice inlet. In fact, it can be shown using the ambipolar diffusion framework that a peak in plasma density cannot exist within the insert region plasma volume without a spatial variation in neutral pressure or electron temperature. Rather than complicate the analytical solution further, and in the absence of a good model for the ion flux into the insert region from the orifice, we impose the zero flux condition in order to bound the attachment length to its likely minimum value and capture its scaling with cathode operating conditions. While the predicted attachment length cannot be used directly for the

detailed design of a hollow cathode, it provides insight into the physical mechanisms behind the variation of the attachment length inside hollow cathodes for a wide variety of operating conditions (both low and high currents and mass flow rates). While the assumptions of zero flux along the orifice inlet plane and constant neutral pressure in the insert region may be challenged for cathodes with large orifice-to-insert diameter ratio, ambipolar diffusion theory is broadly applicable to most cathode plasma conditions. Two outlying cases for which our approach will not perform well are relevant to discuss, that of large orifice-to-insert diameter ratio ($\bar{r} \sim 1$) and small orifices at high pressure (pressure-diameter product for the insert $P_g d \gg 10$ Torr-cm and for the orifice $P_g d \sim 1$ Torr-cm). In the limit as $\bar{r}$ approaches 1, the geometry becomes that of a single-channel or tube hollow cathode, and because the insert and orifice have the same diameter the constant-pressure assumption implies that the orifice and insert $P_g d$ should be identical. This would cause the solution to revert to the single-eigenmode solution of the orifice, which results in an axially uniform plasma density (infinite attachment length, L_{eff}). Such a cathode would likely have strong axial pressure gradients throughout, requiring the inclusion of the relevant terms in the ambipolar diffusion equation. In the other limit, for cathodes with small orifices operated at high pressure, the constant-pressure assumption is more likely to hold in the region upstream of the orifice. The plasma density may be concentrated in the orifice itself, rather than in the insert region. For this case, the plasma density decay in the insert region may no longer be representative of the density distribution. In addition to bounding the minimum value of the attachment length, the final assumption also gives us an independent expression with which to self-consistently solve for the insert electron temperature without relying on a solution that uses only the lowest-order eigenmode as in [27]. Continuity between the insert- and orifice-region plasmas along with a given, strictly positive functional form for the density decay away from the orifice in the radial direction are necessary to extend the Dirichlet boundary condition along the entire insert-region downstream boundary. If we were not to make this assumption, obtaining an analytical solution by standard partial differential equation techniques would not be feasible.

3. One-Dimensional Radial Ambipolar Diffusion

We treat the orifice plasma as axially uniform and consider only the radial variation. Spatial representation beyond a volume-averaged value of the orifice density is important because the orifice solution is later included as a boundary condition for the insert solution; a full 2-D representation of the orifice plasma, however, would require boundary information beyond what can be obtained from a power balance. The steady-state density in a cylindrical geometry can be found from the time-independent ambipolar diffusion equation: [27]

$$\frac{d^2 n_e}{dr^2} + \frac{1}{r}\frac{dn_e}{dr} + \frac{\nu_{iz}}{D_a} n_e = 0, \tag{1}$$

where n_e is the plasma density, ν_{iz} is the ionization rate, and D_a is the ambipolar diffusion coefficient. The ambipolar diffusion coefficient is given by:

$$D_a = \frac{e\,(T_{eV} + T_{iV})}{M n_g \sigma_{\text{CEX}} v_{i,th}}, \tag{2}$$

where σ_{CEX} is the cross section for resonant charge exchange for the propellant species, n_g is the neutral number density, and $v_{i,th}$ is the ion thermal velocity. Equation (1) can be written in terms of a normalized radius:

$$\frac{d^2 n_e}{d\bar{r}^2} + \frac{1}{\bar{r}}\frac{dn_e}{d\bar{r}} + \gamma^2 n_e = 0, \tag{3}$$

where $\bar{r} = r/R$, R is the insert radius, and

$$\gamma^2 = R^2 \frac{n_g \sigma_{iz} \bar{v}}{D_a}. \tag{4}$$

In Equation (4), σ_{iz} is the Maxwellian-averaged ionization cross section for ground-state neutrals by electron impact, and $\bar{v}$ is the average electron velocity. In the orifice region, γ should be evaluated using orifice properties but retain the normalization with respect to the *insert* radius. This is required in order to maintain compatibility between the orifice and insert eigenfunctions when the orifice solution is applied as a boundary condition in the insert region.

The parameter γ is defined by the ratio of ion production to losses due to ambipolar diffusion, and is roughly equivalent to the second Damköhler number for the ionization reaction. Due to the inverse relationship between D_a and n_g it can be shown that, for a given gas species and heavy-particle temperature, γ varies only with T_{eV} and the product $n_g R$ (or neutral pressure-diameter product, $P_g d$). Considering that $\gamma \sim 1$ and is the only parameter that appears in Equation (3), we can immediately ascertain the importance of $P_g d$ to the solution.

When γ is small, diffusion losses are large with respect to ion production. This creates a more uniform ion density (ions are more quickly spread throughout the volume than they are produced). When γ is large, ion production occurs faster than diffusion, and the density will be more "peaked" in the radial direction, with stronger density gradients toward the boundaries. This parameter also specifies the number of ions that

must be produced for each ion in the volume in order to maintain the existing plasma density. For xenon gas, $\gamma\bar{r}_o$ increases from approximately 0.7 to 2.4 as $P_g d$ increases from 0.1 to 10 Torr-cm. Due to the differences in normalization and solution dimension between the orifice and insert regions, respectively, γ in the orifice depends on $\bar{r}_o$, while γ in the insert region does not. For the 2-D insert solution described in Section 4, γ increases from approximately 0.85 to 2.0 as $P_g d$ increases from 0.1 to 10 Torr-cm for xenon.

3.1. General solution

Equation (3) is a Helmholtz equation with unknown eigenvalue, γ. In radial coordinates with $\bar{r} \in [0, \bar{r}_o]$ (where $\bar{r}_o$ would be replaced by 1 in the insert region) the bounded, nontrivial form of the solution is a zeroth-order Bessel function of the first kind,

$$n_e = C J_0 \left(\gamma \bar{r}\right), \tag{5}$$

where C is a proportionality constant.

Previous authors [27] have used a homogeneous Dirichlet boundary condition at the wall, $n_e\left(\bar{r} = \bar{r}_o\right) = 0$ (again replacing $\bar{r}_o$ with 1 if applied in the insert region). This boundary condition is valid for sufficiently high-pressure discharges. [54] Examples of this case include the NSTAR neutralizer cathode [27] and cathodes with small orifice-to-insert diameter ratios [59], which operate at pressures in excess of 100 Torr. A Robin boundary condition is more appropriate in the context of most hollow cathodes, where the insert and orifice pressures are typically within the range of 1 to 10 Torr. The Robin boundary condition enforces flux continuity at the plasma-sheath boundary and equates the Bohm and diffusion fluxes:

$$-D_a \frac{dn_e}{dr} = n_e v_B \Leftrightarrow \frac{dn_e}{d\bar{r}} + n_e \delta = 0, \tag{6}$$

where $\delta = v_B R / D_a$ and can be interpreted as a measure of the ratio of the Bohm (advective) velocity to the average radial diffusion velocity (a plasma analogue of the Péclet number). This parameter, like γ, varies only with $n_g R$ (or $P_g d$) and T_{eV} for a given gas species and heavy-particle temperature. Unlike γ, however, δ should be evaluated using the local radius for the region considered (i.e., $R = r_o$ for the orifice). The parameter δ is typically ~ 10, varies approximately linearly with $P_g d$ due to its weak dependence on T_{eV}, and governs the slope of the density gradient near the solution boundary. In conjunction with γ, δ causes similar changes in the plasma density solution with $P_g d$; for increasing $P_g d$, near-boundary gradients in density become larger, and at smaller $P_g d$ the density profile becomes more uniform.

Both Dirichlet and Robin boundary conditions generate an infinite set of positive, increasing eigenvalues. The Dirichlet boundary condition requires $\gamma\bar{r}_o$ to be a zero of J_0, while the Robin boundary condition yields the following transcendental equation for γ:

$$-\gamma\bar{r}_o J_1\left(\gamma\bar{r}_o\right) + \delta J_0\left(\gamma\bar{r}_o\right) = 0. \tag{7}$$

Because we do not have inhomogeneous Dirichlet information along any boundary of the orifice and we assumed our solution was one-dimensional, we retain only the first eigenmode for the solution — retaining further terms would render the coefficients of the eigenmodes impossible to determine. This allows us to compute the maximum electron temperature for the orifice region with Equation (4) and the smallest γ found using Equation (7). For a single eigenmode, the electron temperature cannot exceed this value with a strictly positive plasma density. The same procedure can be used to determine the maximum permissible electron temperature in the insert region. However, we do not use this value as the insert electron temperature as we do in the orifice solution; imposing this value results in non-decaying solutions that do not satisfy the upstream boundary conditions.

We observe that the electron temperature, and therefore the plasma density profile, depend only on the product of the neutral density and radius (or $P_g d$) of the region of interest. If we have a fixed value of the heavy particle temperature, we can calculate the electron temperature for both types of boundary condition in terms of $P_g d$, as shown in Figure 1. Both boundary conditions yield identical solutions in the high-pressure limit, and above $P_g d = 1$ Torr-cm the two solutions for T_{eV} differ by less than 5%. We assume the more general case of the Robin boundary condition for the remainder of this paper.

3.2. Orifice

For the single-eigenmode orifice solution, the proportionality constant in Equation (5) corresponds to the maximum density in the orifice, n_{or}, which is computed from the average density:

$$\bar{n}_e = \frac{\int_0^{\bar{r}_o} n_{or} J_0\left(\gamma s\right) s \, \mathrm{d}s}{\pi \bar{r}_o^2} \Leftrightarrow n_{or} = \frac{\gamma \bar{r}_o}{2 J_1\left(\gamma \bar{r}_o\right)} \bar{n}_e. \tag{8}$$

The average density is determined using the power balance from [27]:

$$R_p I_d^2 = \frac{5}{2} I_d \left(T_{eV} - T_{eV}^{\mathrm{ins}}\right) + n_g \bar{n}_e e \langle \sigma_{iz} v_e \rangle \epsilon_i \left(\pi r_o^2 L_o\right), \tag{9}$$

where R_p is the plasma resistance, L_o is the orifice length, I_d is the total cathode discharge current, T_{eV} is the electron temperature, n_g is the neutral density in the orifice, and ϵ_i is the total ionization energy.

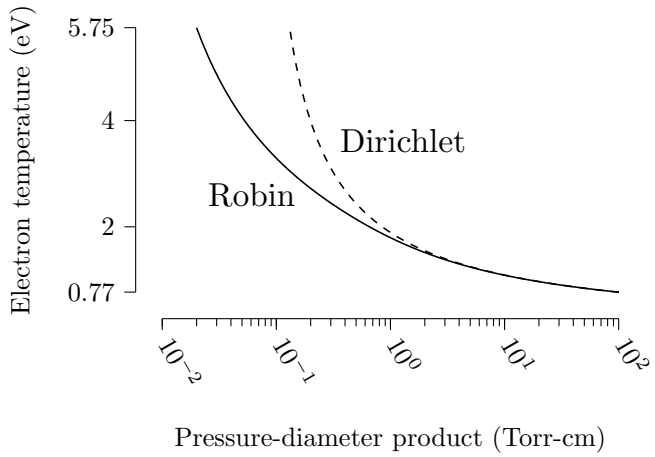

Figure 1. Dependence of electron temperature on the pressure-diameter product expressed in Torr-cm for both forms of radial boundary condition with T_i fixed at 3000 K. Adapted from "Christopher J. Wordingham *et al.*, *Theoretical Prediction of the Dense-Plasma Attachment Length in an Orificed Hollow Cathode,* 35th International Electric Propulsion Conference, 2017, IEPC-2017-566 [60]." Copyright 2017, Christopher J. Wordingham *et al.*

The plasma resistance is calculated with the plasma resistivity and orifice geometry:

$$R_p = \eta_p \frac{L_o}{\pi r_o^2}. \tag{10}$$

The resistivity, η_p, is computed based on the electron-ion and electron-neutral collision frequencies and the average electron density (because the exact distribution of the current density within the orifice plasma is unknown):

$$\eta_p = \frac{m}{\bar{n}_e e^2} \left(\nu_{ei} + \nu_{en}\right). \tag{11}$$

The electron-ion collision frequency is calculated using:

$$\nu_{ei} = 2.9 \times 10^{-12} \bar{n}_e \frac{\ln \Lambda}{T_{eV}^{3/2}}. \tag{12}$$

Both the electron-neutral and ionization reaction rates rely on Maxwellian-averaged cross sections calculated using Hayashi's most recent data [61]. The Coulomb logarithm is given by:

$$\ln \Lambda = 23.0 - \frac{1}{2} \ln\left(10^{-6} \bar{n}_e T_{eV}^{-3}\right). \tag{13}$$

4. Insert Region Ambipolar Diffusion

We consider the two-dimensional, axisymmetric diffusion equation with a source term corresponding to volumetric ionization to compute the steady-state plasma density in the insert region. Using normalized coordinates $\bar{r} = r/R$ and $\bar{z} = z/R$, this equation may be written as:

$$\frac{\partial^2 n_e}{\partial \bar{r}^2} + \frac{1}{\bar{r}} \frac{\partial n_e}{\partial \bar{r}} + \frac{\partial^2 n_e}{\partial \bar{z}^2} + \gamma^2 n_e = 0. \tag{14}$$

The value of γ is found using the value of T_{eV} from the flux condition at the orifice plate discussed in the following section.

4.1. Boundary conditions

The insert region is axisymmetric with a Robin boundary condition at the insert surface (Equation (6)) and a homogeneous Neumann boundary condition on the centerline to enforce symmetry about the cathode axis. In the axial direction, the extent of the solution domain is assumed to be infinite, so the solution must be bounded as $\bar{z} \to -\infty$ upstream of the orifice. Different sets of boundary conditions at $\bar{z} = 0$ may be used to represent the boundary value problem, with two cases shown in Figure 2. The most general representation, Figure 2(a), includes an additional Robin boundary condition on the orifice plate surface and a Dirichlet condition enforcing continuity with the orifice solution along the orifice inlet. This piecewise-defined boundary condition prevents the use of standard partial differential equation techniques such as separation of variables and requires numerical techniques. To obtain an analytical solution, we propose a simplification of the boundary condition on the orifice plate, as shown in Figure 2(b).

The boundary condition for $\bar{z} = 0$ and $\bar{r} \in [0, \bar{r}_o]$ is represented by the orifice solution. This solution is extended for $\bar{r} \geq \bar{r}_o$ by imposing three constraints:

1. The extension is C^0 at $\bar{r} = \bar{r}_o$.
2. The extension is C^1 at $\bar{r} = \bar{r}_o$.
3. The extension verifies the boundary condition imposed at $\bar{r} = 1$.

These three constraints can be used with any functional representation of the density that is strictly positive and that features up to three parameters. The first two conditions ensure that the density and the radial flux are continuous at the orifice edge, and the third constraint ensures that the extended function can be represented by the solutions of the eigenvalue problem.

A polynomial form of the density extension can be found that satisfies the first three constraints above, but this representation can yield negative densities. Negative densities can be avoided with a linear representation of the density, although the C^1 condition cannot then be enforced. We propose instead the use of an exponential decay to satisfy these requirements. The density at $\bar{z} = 0$ is represented by:

$$n_e\left(\bar{r}, 0\right) = f\left(\bar{r}\right) = \begin{cases} n_{or} J_0\left(\gamma_{or} \bar{r}\right), \bar{r} \leq \bar{r}_o \\ a \exp\left(b\bar{r}\right) + c, \bar{r} \geq \bar{r}_o \end{cases}, \tag{15a}$$

where the subscript *or* denotes orifice quantities. The imposed constraints form a non-linear system for the

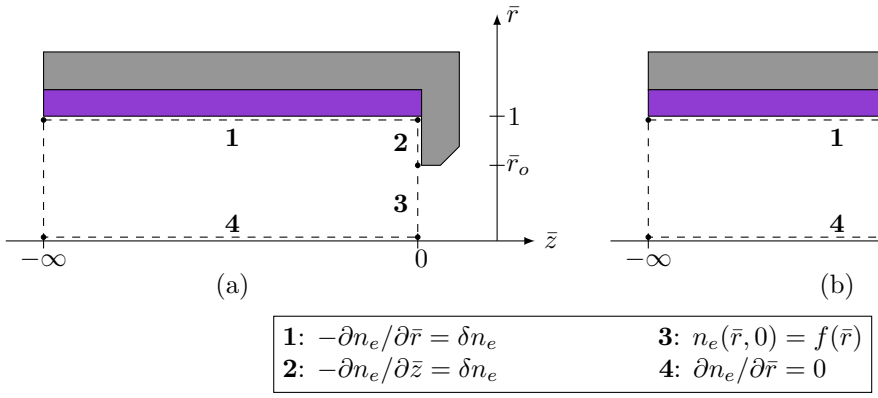

Figure 2. Mathematical representation of the insert region for two different cases: (a) General case with piecewise boundary condition at $z = 0$ and (b) Infinite-length insert with continuous boundary condition. Reproduced from "Christopher J. Wordingham *et al.*, *Theoretical Prediction of the Dense-Plasma Attachment Length in an Orificed Hollow Cathode,* 35th International Electric Propulsion Conference, 2017, IEPC-2017-566" [60]. Copyright 2017, Christopher J. Wordingham *et al.*

continuation function coefficients. We give the case for the Robin boundary condition below:

$$a\exp\left(b\bar{r}_o\right) + c - J_0\left(\gamma_{or}\bar{r}_o\right) = 0 \;\; (C^0) \tag{16a}$$

$$ab\exp\left(b\bar{r}_o\right) + \gamma_{or}J_1\left(\gamma_{or}\bar{r}_o\right) = 0 \;\; (C^1) \tag{16b}$$

$$ab\exp\left(b\right) + \delta\left(a\exp\left(b\right) + c\right) = 0 \;\; (\text{Robin}). \tag{16c}$$

The non-linear system is solved using the Newton-Krylov solver implemented in the Scipy library [62]. It can be shown that for this particular choice of the continuation function, the system of coefficient expressions can be reduced to a single non-linear equation for one of the coefficients:

$$\left(\frac{b}{\delta} + 1\right)\exp b = \left(\frac{b}{\delta_{or}}\bar{r}_o + 1\right)\exp\left(b\bar{r}_o\right), \tag{17}$$

which can then be substituted to obtain the remaining values,

$$a = -\frac{\gamma_{or}J_1\left(\gamma_{or}\bar{r}_o\right)}{b\exp\left(b\bar{r}_o\right)}, \text{ and} \tag{18a}$$

$$c = J_0\left(\gamma_{or}\bar{r}_o\right) + \frac{\gamma_{or}}{b}J_1\left(\gamma_{or}\bar{r}_o\right). \tag{18b}$$

In order to self-consistently obtain the electron temperature, we cannot use the temperature from the single-eigenmode approximation as used in [27]. To obtain the electron temperature and restrict our focus to the *minimum* attachment length, we impose the condition that the total net flux to/from the orifice and orifice plate must be zero. Viewed from a 1-D axial perspective, this ensures that the maximum radially averaged density occurs at the orifice, yielding strictly decaying solutions. The solution of Equation (14) obtained with this approach should satisfy flux conditions on both the orifice plate and orifice hole at $\bar{z} = 0$:

$$\begin{cases} \Phi_{or} = 2\pi R\displaystyle\int_0^{\bar{r}_o}\left(-D_a\frac{\partial n_e}{\partial \bar{z}}\right)s\,\mathrm{d}s \le 0, \text{ for } \bar{r} \le \bar{r}_o \\ \Phi_{pl} = 2\pi R\displaystyle\int_{\bar{r}_o}^{1}\left(-D_a\frac{\partial n_e}{\partial \bar{z}}\right)s\,\mathrm{d}s \ge 0, \text{ for } \bar{r}_o \le \bar{r} \le 1 \\ \Phi_{pl} + \Phi_{or} = 0 \end{cases}$$

The first two expressions must be checked to ensure that the choice of continuation function can generate a solution for which the flux to the orifice plate takes a physically justified direction. $\Phi_{pl} < 0$ would imply that ions were entering the insert region *from* the orifice plate. A side-effect of this condition on the $\bar{z} = 0$ surface is that the plasma density profile in the insert cannot support an ion flux into the orifice region, so a peak density occurring upstream of the orifice inlet surface will not be captured.

4.2. Analytical solution

Using the choice of boundary conditions represented in Figure 2(b) and described above, we solve Equation (14) using separation of variables:

$$n_e = R\left(\bar{r}\right)Z\left(\bar{z}\right).$$

The Robin boundary condition at $\bar{r} = 1$ gives a condition on the eigenvalues of the problem, and the application of both the inhomogeneous Dirichlet boundary condition at $\bar{z} = 0$ and $n_e \to 0$ as $\bar{z} \to -\infty$ allows for the computation of the unknown coefficients for the solution.

Eigenfunctions We obtain the solution for each eigenmode,

$$\phi_k\left(\bar{r}, \bar{z}\right) = C_k J_0\left(\lambda_k\bar{r}\right)\exp\left(\alpha_k\bar{z}\right), \tag{19}$$

where α_k is the separation constant, $\lambda_k^2 = \gamma^2 + \alpha_k^2$, and C_k is the coefficient for each eigenmode. The

separation constant is strictly positive and real, as other cases yield non-vanishing densities for $\bar{z} \to -\infty$.

Separation constant The boundary condition at $\bar{r} = 1$ yields the eigenvalues λ_k and therefore the corresponding separation constants α_k. In the case of a Robin boundary condition, the λ_k satisfy the transcendental equation

$$\frac{D_a \lambda_k J_1(\lambda_k)}{R} = v_B J_0(\lambda_k) \Leftrightarrow \lambda_k J_1(\lambda_k) = \delta J_0(\lambda_k), \quad (20)$$

where $\delta = v_B R / D_a$. Equation (20) yields an infinite number of increasing and unique eigenvalues. The superposition of all eigenmodes gives the solution of the diffusion equation:

$$n_e(\bar{r}, \bar{z}) = \sum_{k=1}^{+\infty} C_k J_0(\lambda_k \bar{r}) \exp(\alpha_k \bar{z}) \quad (21)$$

Eigenmode coefficients The constants C_k are determined with the Dirichlet boundary condition at $\bar{z} = 0$ and the orthogonality of the Bessel functions:

$$\sum_{k=1}^{+\infty} C_k J_0(\lambda_k \bar{r}) = \begin{cases} n_{or} J_0(\gamma_{or} \bar{r}), \ \bar{r} \leq \bar{r}_o \\ f_c(\bar{r}), \ \bar{r} \geq \bar{r}_o \end{cases} \quad (22)$$

where $f_c(s)$ is the continuation function. Multiplying Equation (22) by $\bar{r} J_0(\lambda_m \bar{r})$ and integrating for $\bar{r} \in [0, 1]$ yields:

$$\begin{aligned} C_m = & \frac{1}{\int_0^1 s J_0(\lambda_m s)^2 \, \mathrm{d}s} \\ & \times \left(\int_0^{\bar{r}_o} s n_{or} J_0(\gamma_{or} s) J_0(\lambda_m s) \, \mathrm{d}s \right. \\ & + \left. \int_{\bar{r}_o}^1 s f_c(s) J_0(\lambda_m s) \, \mathrm{d}s \right) \end{aligned} \quad (23)$$

The integration may be carried out analytically excluding the integral involving the continuation function:

$$\begin{aligned} C_m = & \frac{2}{J_0^2(\lambda_m) + J_1^2(\lambda_m)} \\ & \times \left[\frac{n_{or} \bar{r}_o}{\gamma_{or}^2 - \lambda_m^2} (\gamma_{or} J_0(\lambda_m \bar{r}_o) J_1(\gamma_{or} \bar{r}_o) \right. \\ & - \lambda_m J_0(\gamma_{or} \bar{r}_o) J_1(\lambda_m \bar{r}_o)) \\ & + \left. \int_{\bar{r}_o}^1 s f_c(s) J_0(\lambda_m s) \, ds \right] \end{aligned} \quad (24)$$

The remaining integral is calculated numerically.

4.3. Insert electron temperature

As mentioned earlier, we use the electron temperature which balances the total particle flux from the orifice, Φ_{or}, with the total flux to the orifice plate, Φ_{pl}. The decaying solutions obtained represent the minimum attachment length, assuming that the net flux of ions across the orifice inlet is into the insert region. This likely restricts the applicability of our solution to cathodes with relatively constricted orifices, but this is consistent with our assumption of a narrow orifice in the orifice density solution. In order to find the full solution, we calculate the solution for an arbitrary T_{eV}, then iterate until the flux boundary condition is met.

4.4. Algorithm

For a given electron temperature and the required inputs of pressure and heavy particle temperature in each region, the diffusion equation is solved using the following algorithm:

1. The electron temperature for the orifice is calculated from the first eigenmode of the 1-D radial diffusion problem (Equation (7)).
2. The average and peak densities in the orifice are determined with Equations (8) and (9), respectively, and the continuation function is also generated.
3. The insert electron temperature is used to calculate the ambipolar diffusion coefficient, Bohm velocity (or δ), and γ for the insert region plasma.
4. The eigenvalues for the insert problem are computed using Equation (20).
5. The coefficients of each eigenmode are calculated using Equation (24).
6. The series of eigenfunctions is computed with a truncated sum because $C_m \to 0$ as $m \to +\infty$.
7. The orifice and orifice plate fluxes are calculated to determine whether the choice of insert electron temperature satisfies the boundary condition at $\bar{z} = 0$.
8. If the solution does not satisfy the boundary condition in step 7, a new electron temperature is chosen and the procedure is repeated until the correct electron temperature is found using a bisection algorithm.

5. Results and discussion

We compare the results of our approach to the density measurements along the cathode main axis from [9] and with the methodology outlined in [27]. We use neutral gas pressures of 4.5 and 7.8 Torr in the orifice and insert regions, respectively, and a heavy particle temperature of 3000 K in both regions. The values were chosen to coincide with the inputs used in [27].

5.1. Verification

The coefficients calculated from Equation (24) decay as λ_m increases with m. Figure 3 shows the eigen-coefficients for $m \leq 50$. The solution we propose

features multiple prominent eigenmodes, though most of them decay rapidly. It is important that we have used the sum over multiple eigenmodes, as we can see that the fundamental eigenmode does not necessarily have the largest coefficient due to the constricted shape of the orifice solution compared to the fundamental mode in the insert region. In addition, a single-eigenmode solution in the insert region clearly cannot meet the boundary conditions imposed by the presence of the orifice.

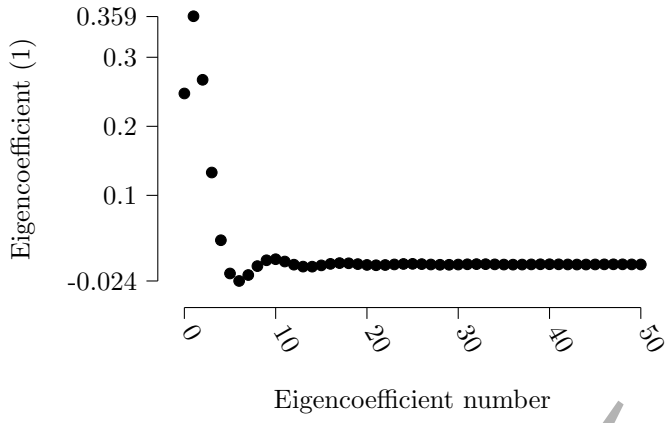

Figure 3. Eigencoefficients C_k. Adapted from "Christopher J. Wordingham *et al.*, *Theoretical Prediction of the Dense-Plasma Attachment Length in an Orificed Hollow Cathode,* 35th International Electric Propulsion Conference, 2017, IEPC-2017-566 [60]." Copyright 2017, Christopher J. Wordingham *et al.*

We also verify that the solution on the $\bar{z} = 0$ surface follows the imposed Dirichlet boundary condition. Figure 4 shows the normalized density as a function of normalized radius, along with the imposed Dirichlet boundary condition. We have excellent agreement with the imposed condition from Equation (15a), and we observe that the proposed extension is indeed C^0 and C^1 at $\bar{r} = \bar{r}_o$. The Robin condition at $\bar{r} = 1$ results in a small, yet non-zero, derivative at the wall, as opposed to the solution for the homogeneous Dirichlet condition, for which a strong density gradient is expected. Another important side-effect of the Robin condition is that the plasma density at the sheath edge is readily calculated from the solution, which is necessary for accurately calculating the fluxes to the insert. The Dirichlet condition, on the other hand, artificially increases the flux to the wall for all but very high pressures and makes the calculation of the density at the sheath edge problematic; an infinite velocity is required for finite flux at zero density.

The results of imposing the exponential extension can be validated using a 2-D numerical solution that includes the Bohm flux condition instead of an imposed radial density profile along the orifice plate

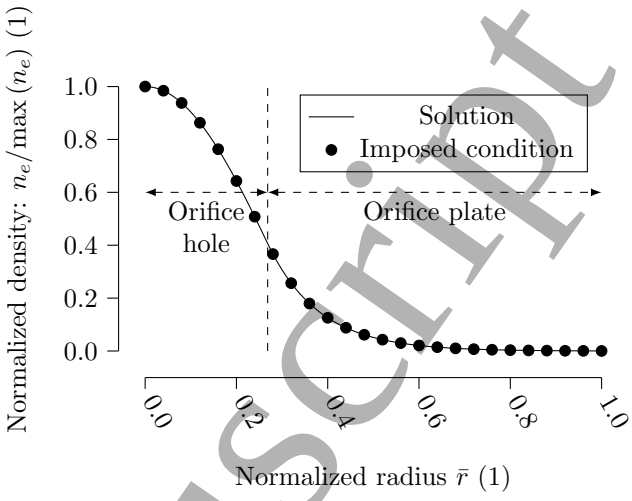

Figure 4. Verification of the imposed Dirichlet boundary condition. Adapted from "Christopher J. Wordingham *et al.*, *Theoretical Prediction of the Dense-Plasma Attachment Length in an Orificed Hollow Cathode,* 35th International Electric Propulsion Conference, 2017, IEPC-2017-566 [60]." Copyright 2017, Christopher J. Wordingham *et al.*

surface. We show in Figure 5 the radial density profiles as obtained from the exponential extension, a 2-D numerical solution of the ambipolar diffusion equation where the Bohm flux is imposed on the orifice plate, and 2-D fluid simulation from [44].

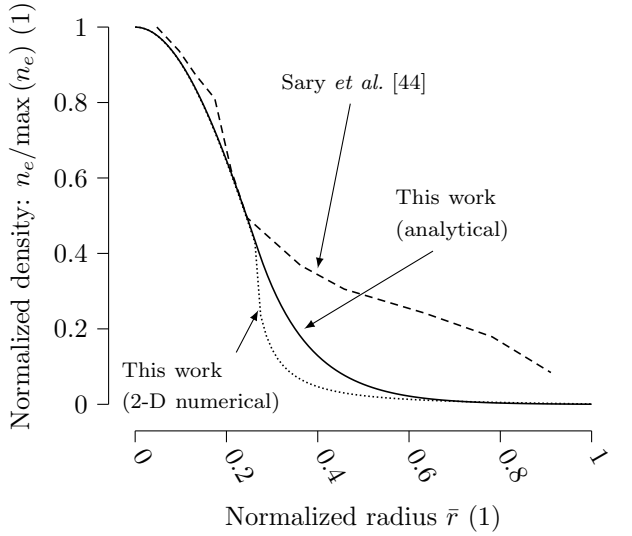

Figure 5. Comparison of radial density profiles. The results of Sary *et al.* for the $\bar{z} = 0$ surface were recovered from contour plots in [44].

Using a parametric study, however, we have found that the exponential extension, *for certain combinations of orifice and insert* $P_g d$, can produce erroneous

results especially when the orifice $P_g d$ is much smaller than the insert $P_g d$. Using the same analytical approach, we have found that applying a homogeneous Dirichlet boundary condition ($n_e(\bar{r}) = 0$) along the orifice plate surface produces more reliable results over a wide range of input parameters. As such, we apply the exponential extension for the density profile validation, but use the simpler $n_e(\bar{r}) = 0$ condition to derive scaling relationships for the electron temperature and attachment length. This boundary condition on the orifice plate should also represent a worst-case for the flux to the plate surface and, due to the zero-flux condition along the $\bar{z} = 0$ surface, a worst-case for the density derivative at the orifice inlet surface. This should result in a lower bound for the attachment length.

5.2. Sensitivity analysis

Because the only required inputs for our analytical approach are the neutral densities and heavy particle temperatures in each region (excluding the cathode geometry), and the pressures are generally determined using measurements or flow models, we must determine the sensitivity of the solution to the ion temperature. The variation in the solution result for different heavy particle temperatures is shown in Figure 6. The shape of the solution remains relatively constant when the ion temperature varies by ±1000 K (±33%) from the nominal value of 3000 K, though the resulting electron temperature varies by less than ±8%.

5.3. Density profile

Our 2-D approach allows for the computation of the plasma density on the entire domain. Figure 7 shows a contour plot of the density calculated for the NSTAR cathode, with an insert pressure of 7.8 Torr and a discharge current of 15 A. The contour features qualitative agreement with previous numerical results for various cathodes and operating regimes as described in [34, 39, 40, 63, 64].

We compare the axial plasma density calculated using our approach to experimental data [9] and to the results calculated using the semi-empirical model described in [27] in Figure 6. Both our analytical approach and the semi-empirical model accurately predict the density decay rate, but neither is able to capture the increase in density upstream of the orifice. Near-orifice changes in neutral pressure and electron temperature that likely occur are not included in either representation of the cathode plasma. These effects, along with the chosen boundary conditions, cause both methods to underpredict the experimental plasma density. In the case of our approach, the assumption of zero net ion flux across the orifice plane

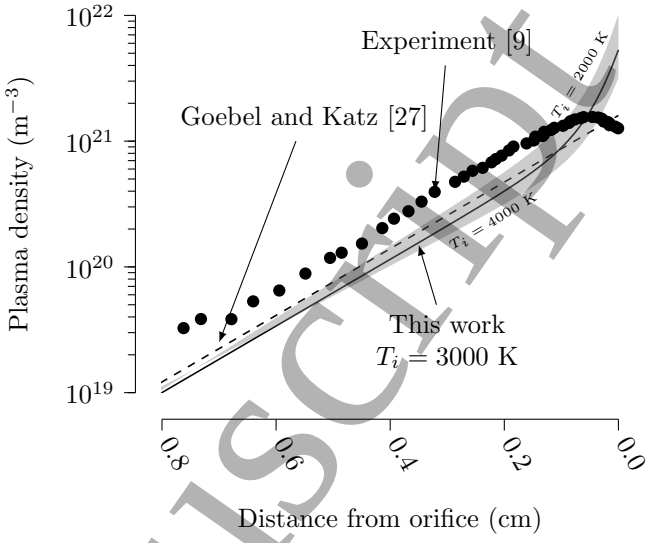

Figure 6. Numerical results for the axial plasma density profile for varying ion temperature (2000–4000 K) and comparison to previous modeling [27] and experimental results [9] for the NSTAR discharge cathode operating at I_d = 15 A. Adapted from "Christopher J. Wordingham *et al.*, *Theoretical Prediction of the Dense-Plasma Attachment Length in an Orificed Hollow Cathode,* 35th International Electric Propulsion Conference, 2017, IEPC-2017-566 [60]." Copyright 2017, Christopher J. Wordingham *et al.*

surface also causes an effective downstream "shift" in the plasma density solution. In the case of Goebel and Katz's single-eigenmode solution, it is only valid in the decaying (upstream) portion of the density profile, and must be normalized by a peak density, resulting in a similar effect if the density chosen is the peak orifice density.

The most important difference between the two approaches is that our method only requires the pressures and heavy particle temperatures as inputs, while the semi-empirical model requires knowledge of the ion current generated within the insert region.

It is relevant to mention a limitation of our approach: given that the operator and boundary conditions do not depend on the discharge current, with the exception of the scaling of the orifice peak density, a theoretical framework of this form cannot directly capture the experimentally observed trend of decreasing attachment length with increasing discharge current. However, the entire operator for the 2-D solution can be shown to depend predominantly on the insert $P_g d$ (including the exponential extension coefficients), and the effects of γ and δ on the form of the solution are similar to those described for the 1-D solution. The plasma density in the 2-D solution also depends on the discharge current through the peak density from the orifice solution, but this only

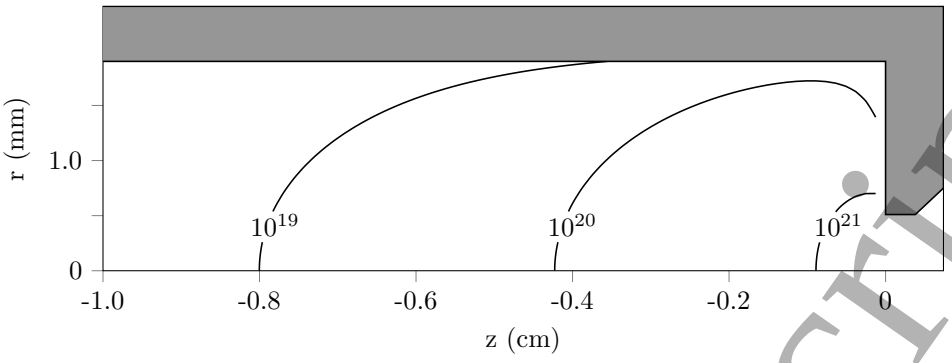

Figure 7. Plasma density contour (m^{-3}) for the NSTAR cathode operating at I_d = 15 A. Reproduced from "Christopher J. Wordingham *et al.*, *Theoretical Prediction of the Dense-Plasma Attachment Length in an Orificed Hollow Cathode,* 35th International Electric Propulsion Conference, 2017, IEPC-2017-566 [60]." Copyright 2017, Christopher J. Wordingham *et al.*

contributes a multiplicative scale factor to the entire profile and does not affect γ or δ.

The attachment length, therefore, depends on the discharge current and orifice diameter only indirectly through their effects on the *total pressure*. This dependence on the total pressure has been suggested by early work on mercury-fed cathodes by Siegfried and Wilbur, [21] in which the attachment length was shown to be insensitive to changes in the orifice size and discharge current if the total pressure was held constant. The only apparent methods to diagnose the direct dependence of attachment length or electron temperature on discharge current or orifice size would be to model the effect on the insert region neutral pressure or to model the change in the Bohm velocity at the insert boundary with changes in emission current density.

5.4. Attachment length

The experimental attachment length is derived from the measured electron density profile. Because we — following [27] — define the attachment length as the length-scale of the exponential decay of the electron density upstream of the cathode orifice, we fit only the relevant portion of the experimental data with a decaying exponential. We show an example of this approach in Figure 8. The attachment length is derived from the experimental data through a log-linear fit of the exponential plasma density decay. Figure 8 shows this portion of the plasma density decay, which can be well-approximated as an exponential, and against which we compare the results of our approach. This region is upstream of and away from the cathode orifice and any near-orifice effects. Because the first-order eigenmode decays over the longest distance (other eigenmodes quickly decay upstream of the near-orifice region), we use this term to evaluate the attachment length. Our data were obtained from the open literature [9, 10, 18, 25, 40, 65] that contains

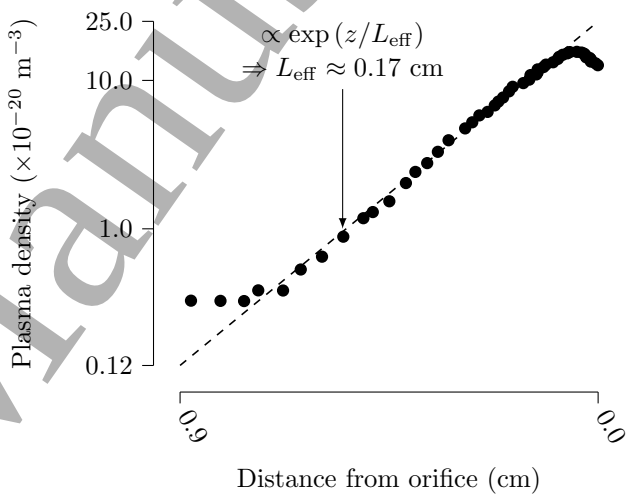

Figure 8. Example of the derivation of the attachment length from an experimentally measured electron density profile. Experimental data from [9] for the NSTAR discharge cathode operating at 15 A. Reproduced from "Pierre-Yves C. R. Taunay, *Scaling Laws in Orificed Thermionic Hollow Cathodes,* Ph.D. dissertation, Princeton University, 2020 [33]." Copyright 2020, Pierre-Yves C. R. Taunay.

the necessary information to use our approach (*i.e.*, measurements of the total pressure, electron density, and relevant geometry). The data span a range of discharge currents of 2–100 A, mass flow rates of 1.8–13 sccm of xenon, and orifice-to-insert diameter ratios of 0.2–0.7. We have assembled a database of publicly available cathode experimental data [66] and a permanent identifier is shown in the Data Availability section of this manuscript.

Error analysis The NSTAR, NEXIS, and JPL lanthanum hexaboride cathodes share the same experimental setup and diagnostics for which the error in the density measurement was reported [49] to be

$\pm 40\%$ ($\sigma_n^2 = 0.04$). For the density measurements taken by Salhi [25] no experimental uncertainty was reported so we assume the same value of $\pm 40\%$. The error inherent in performing the various steps of the linear regression on the logarithm of the density must also be estimated to obtain a confidence interval for the derived attachment length. If the density at a given point has a variance of $\bar{n}_e^2 \sigma_n^2$ (where $\bar{n}_e$ is the average density at that point) then it can be shown [67] that its logarithm, $Y = \ln n_e$, has a variance of σ_n^2. For the linear fit of $\ln n_e$ with parameters $\hat{\beta}_0$ and $\hat{\beta}_1$, we have

$$\hat{Y} = \hat{\beta}_0 + \hat{\beta}_1 \bar{z}. \tag{25}$$

The inverse of $\hat{\beta}_1$ is the normalized emission length. The standard error of the slope is [68]:

$$\sigma_\beta^2 = \frac{\sigma_n^2}{\sum_{i=1}^{N} (\bar{z}_i - \hat{z})^2}, \tag{26}$$

where $\hat{z}$ is the average distance from the orifice inlet. If we now assume that $\hat{\beta}_1$ is also normally distributed about the value calculated using the regression procedure, then the emission length has a variance (to first order) of:

$$\sigma_L^2 = \frac{\sigma_\beta^2}{\hat{\beta}_1^2}. \tag{27}$$

5.5. Electron temperature

The electron temperature is typically measured as a function of axial position in the insert region. Because the electron temperature varies gradually upstream of the cathode orifice, we use the axial line-average of the experimental data over the entire cathode insert region to obtain a single experimental value, as shown in Figure 10. We take the uncertainty of the electron temperature measurements to be ± 0.5 eV, as reported in [49], unless otherwise specified.

5.6. Scaling Relationships

Using the results of our analytical approach — calculated over a wide range of $\bar{r}_o$ and $P_g d$ — it is possible to obtain approximate, but insightful, expressions for the dependencies of the electron temperature and attachment length on the input operating conditions. The method described in the preceding sections yields an analytical solution for the plasma density within the cathode domain, but due to the transcendental root-finding and bisection procedure required by the solution algorithm, obtaining closed-form solutions in terms of elementary functions for the resulting electron temperature and attachment length is likely not possible. However, by defining the attachment length as the decay length scale of the lowest-order eigenmode of the solution (in units of insert radii):

$$L_{\text{eff}} = \frac{1}{\alpha_0}, \tag{28}$$

we can obtain an approximate relationship for L_{eff} as a function of the neutral $P_g d$ in the insert region. As mentioned in the previous section, the operator governing density evolution in the insert plasma is *almost* solely dependent on the insert neutral pressure-diameter product, $P_g d$. While $\bar{r}_o$ and orifice $P_g d$ potentially affect the solution, it can be shown that the effects of these parameters on electron temperature are negligible, and the effects on attachment length are small. We performed a parametric study using the $n_e(\bar{r}) = 0$ boundary condition along the orifice plate, values of $\bar{r}_o \in \{0.1, 0.2, 0.3, 0.4, 0.5\}$, $P_g d \in [0.1, 10]$ Torr-cm in the insert region, and $P_g d \in [0.01, 10\bar{r}_o]$ Torr-cm in the orifice region. This study demonstrated that there is essentially no effect of the normalized orifice size or orifice $P_g d$ on either the attachment length or electron temperature. The effect of orifice size on neutral pressure (which is not considered in our analysis) is likely to have a much greater effect on L_{eff} and electron temperature through the insert $P_g d$ than the independent effect of either $\bar{r}_o$ or orifice $P_g d$. Fitting the calculated attachment length and electron temperature values for xenon gas and the aforementioned range of input parameters yields the following relationships for each as functions of the insert neutral pressure-diameter product in Torr-cm:

$$L_{\text{eff}} = 0.75832 + \frac{0.18239}{(P_g d)^{1.22956}} \tag{29}$$

$$T_{eV} = 0.51897 + \frac{1.21492}{(P_g d)^{0.35322}}. \tag{30}$$

These approximations are shown alongside the calculated values from our approach in Figures 9 and 10. Due to the weakly ionized nature of the cathode insert region plasma, we assume that the neutral $P_g d$ is equal to the measured total pressure. No distinction is made between our results for different values of the non-dimensional orifice radius, $\bar{r}_o$, or the orifice pressure-diameter product due to the insensitivity of the attachment length and electron temperature to these parameters over the range of values presented. The form used for each fit was chosen from a selection of candidate functions: $a + b/\log(x + c)^n$, $a + b/(x + c)^n$ with $n \in 1, .., 6$, along with $a + b/x^c$, a/x (equivalent to the form used by Albertoni [24] for fixed R), $a + bx + cx^2$, and $a + b/x + c/x^2$. In order to select the best fit for out-of-set prediction, K-Fold cross-validation was used with 10 folds in the source data. Using this method, we fit each candidate function to a training set comprised of a random selection of 90% of the source dataset, then calculate

the total squared error for the remaining 10% of the data (the test set); we repeat this method once for each "fold" with different training and test sets and select the fit function with the lowest average total squared error across all folds. We then fit the best candidate function — in this case $a + b/x^c$ for both calculated values — to the entire dataset to obtain the coefficients provided above.

The formula shown in Equation (29) is in units of insert radii. For a given $P_g d$, the dimensional value of the attachment length is obtained from Equation (29) by multiplying it by the insert radius. For the experimental case shown in Figure 8, the total pressure is 8.1 Torr and insert diameter 3.8 mm. [9] Assuming that the neutral pressure is given by the experimentally measured total pressure of 8.1 Torr, we calculate a non-dimensional attachment length of 0.80. The corresponding dimensional value is 0.15 cm, which is within the error bounds of the experimentally determined value of 0.17±0.02 cm shown in Figure 8.

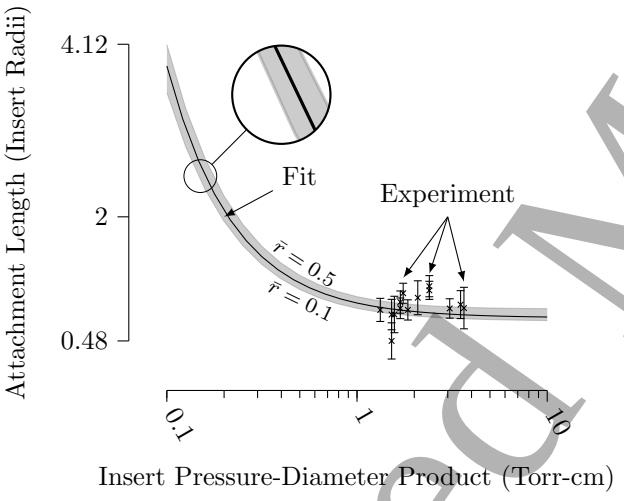

Figure 9. Attachment length as defined in Equation (28), calculated using the analytical solution (thin shaded region) and the approximate functional form given in Equation (29) (line). All available experimental values of the attachment length from [9, 10, 18, 25, 40, 65] are shown as individual points. Adapted from "Pierre-Yves C. R. Taunay *et al.*, *The Influence of Ambipolar Diffusion on the Attachment Length and Electron Temperature in Orificed Hollow Cathodes,* 36th International Electric Propulsion Conference, 2019, IEPC-2019-A628 [69]." Copyright 2019, Pierre-Yves C. R. Taunay *et al.*

Examining these approximate forms, we see that (under the stated assumptions) the density decay length scale and the associated insert plasma electron temperature depend almost exclusively on the neutral pressure-diameter product in the insert region. In addition, while L_{eff} varies substantially for low values of the pressure-diameter product (< 1 Torr-cm), once $P_g d$ reaches approximately 2 Torr-cm, the attachment

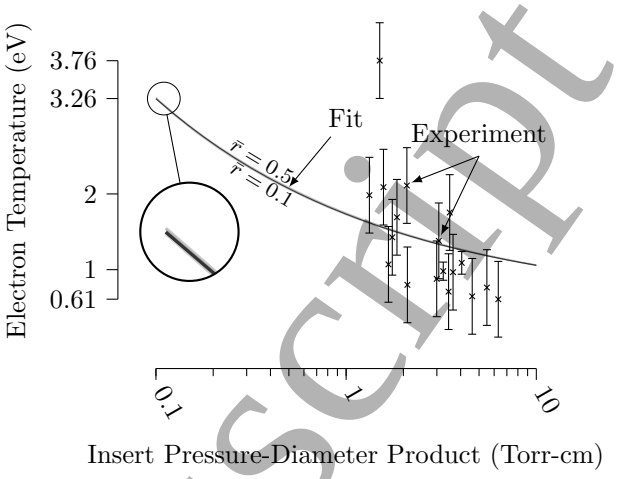

Figure 10. Insert plasma electron temperature calculated using the analytical solution (thin shaded region – obscured by fit line) and the approximate functional form given in Equation (30) (line). All available experimental values of the average insert electron temperature from [9, 10, 18, 25, 40] are shown as individual points. Adapted from "Pierre-Yves C. R. Taunay *et al.*, *The Influence of Ambipolar Diffusion on the Attachment Length and Electron Temperature in Orificed Hollow Cathodes,* 36th International Electric Propulsion Conference, 2019, IEPC-2019-A628 [69]." Copyright 2019, Pierre-Yves C. R. Taunay *et al.*

length changes by only a few percent even for large increases in pressure for a fixed diameter. This suggests that larger insert inner diameters would lead to better utilization of the emission area, especially in the high-pressure limit where our assumptions are most likely to hold. This is consistent with the experimental observation that attachment length increases for a given cathode when operated at lower pressure. [27, 35, 70] In the range of operation for most existing cathodes, 1–10 Torr-cm, the attachment length will generally be on the order of the insert inner radius.

6. Conclusion

We have developed a methodology to analytically determine the plasma density profile (and therefore the attachment length) within the hollow cathode insert region, along with the insert-region electron temperature, using only gas pressure and temperature as inputs. The plasma density profile we calculate compares well to both experimental data and prior modeling efforts for the validation case shown, though near-orifice effects (including the peak in plasma density near the cathode orifice observed experimentally) cannot be captured with the included boundary conditions.

Because it does not rely on experimental data or complex computational methods, our approach can be used to predict the scaling of electron

temperature and attachment length for a wide range of input parameters. Nondimensionalization of the governing equations and evaluation of the solution results over a range of input parameters reveal that the attachment length and electron temperature depend almost exclusively on the insert-region neutral pressure-diameter product. This dependence suggests that any direct influence of orifice size on attachment length or electron temperature is likely small. Rather, changes in orifice size for fixed mass flow rate will affect the pressure-diameter product in the insert region and therefore the plasma properties. Fits to our results yield simple relationships for the variation of electron temperature and attachment length with insert $P_g d$, and suggest that, for fixed operating pressure, high-pressure cathodes should be designed with larger insert inner diameter to make more efficient use of the emitter surface.

Acknowledgments

The authors would like to thank the Princeton Program in Plasma Science and Technology for supporting this work.

Data Availability

The cathode experimental data and software to assemble the corresponding database are openly available at the following DOI: `10.5281/zenodo.3956853`

References

[1] A. Lunk. Plasma activated physical vapour deposition (papvd) by hollow cathode arc (hca). *Vacuum*, 41(7):1965 – 1967, 1990.

[2] Y. S. Kuo, R. F. Bunshah, and D. Okrent. Hot hollow cathode and its applications in vacuum coating: A concise review. *Journal of Vacuum Science & Technology A*, 4(3):397–402, 1986.

[3] H. Morgner, M. Neumann, S. Straach, and M. Krug. The hollow cathode: a high-performance tool for plasma-activated deposition. *Surface and Coatings Technology*, 108-109:513 – 519, 1998.

[4] D. M. Goebel and A. T. Forrester. Plasma studies on a hollow cathode, magnetic multipole ion source for neutral beam injection. *Review of Scientific Instruments*, 53(6):810–815, 1982.

[5] Shigeru Tanaka, Hiroaki Morita, and Junji Sakuraba. Use of a hollow cathode in a DuoPIGatron hydrogen ion source. *Japanese Journal of Applied Physics*, 19(9):1703–1710, sep 1980.

[6] P. P. Deichuli, G. F. Abdrashitov, A. A. Ivanov, V. V. Kolmogorov, V. V. Mishagin, G. I. Shul'zhenko, N. V. Stupishin, D. Beals, and R. Granetz. Ion source with lab6 hollow cathode for a diagnostic neutral beam injector. *Review of Scientific Instruments*, 77(3):03B514, 2006.

[7] A. T. Forrester, D. M. Goebel, and J. T. Crow. Ibis: A hollow-cathode multipole boundary ion source. *Applied Physics Letters*, 33(1):11–13, 1978.

[8] Kristina K. Jameson, Dan M. Goebel, and Ron M. Watkins. Hollow Cathode and Thruster Discharge Chamber Plasma Measurements Using High-Speed Scanning Probes. *29th International Electric Propulsion Conference*, 2005.

[9] Kristina K. Jameson, Dan M. Goebel, and Ronald M Watkins. Hollow cathode and keeper-region plasma measurements. *41st AIAA/ASME/SAE/ASEE Joint Propulsion Conference & Exhibit*, 2005. AIAA-2005-3667.

[10] Emily Chu and Dan M. Goebel. High-current lanthanum hexaboride hollow cathode for 10-to-50-kW hall thrusters. *IEEE Transactions on Plasma Science*, 40(9):2133–2144, 2012.

[11] Dan M. Goebel, Ron M. Watkins, and Kristina K. Jameson. LaB6 Hollow Cathodes for Ion and Hall Thrusters. *Journal of Propulsion and Power*, 23(3):552–558, 2007.

[12] Dan M. Goebel and Ronald M. Watkins. Compact lanthanum hexaboride hollow cathode. *Review of Scientific Instruments*, 81(2010):1–7, 2010.

[13] Dan M. Goebel, Kristina K. Jameson, Ron M. Watkins, Ira Katz, and Ioannis G. Mikellides. Hollow cathode theory and experiment. I. Plasma characterization using fast miniature scanning probes. *Journal of Applied Physics*, 98(11):1–9, 2005.

[14] Ioannis G. Mikellides, Ira Katz, Dan M. Goebel, Kristina K. Jameson, and James E. Polk. Wear Mechanisms in Electron Sources for Ion Propulsion, II: Discharge Hollow Cathode. *Journal of Propulsion and Power*, 24(4):866–879, 2008.

[15] Ioannis G. Mikellides, Ira Katz, Dan M. Goebel, Kristina K. Jameson, and James E. Polk. Wear Mechanisms in Electron Sources for Ion Propulsion, I: Neutralizer Hollow Cathode. *Journal of Propulsion and Power*, 24(4):855–865, 2008.

[16] Dan Goebel, Kristina K Jameson, Ron M. Watkins, and Ira Katz. Hollow Cathode and Keeper-Region Plasma Measurements Using Ultra-Fast Miniature Scanning Probes. *40th AIAA/ASME/SAE/ASEE Joint Propulsion Conference & Exhibit*, 2004.

[17] Michele Coletti and Stephen B Gabriel. Insert Temperature Measurements of a 180A Hollow Cathode for the HiPER Project. *48th AIAA/ASME/SAE/ASEE Joint Propulsion Conference & Exhibit*, 2012.

[18] Paul J. Wilbur. Advanced Ion Thruster Research. Technical Report CR-168340, NASA, 1984.

[19] D. E. Siegfried and P. J. Wilbur. A model for mercury orificed hollow cathodes-Theory and experiment. *AIAA Journal*, 22(10):1405–1412, 1984.

[20] D. Siegfried and P. J. Wilbur. An investigation of mercury hollow cathode phenomena. *13th International Electric Propulsion Conference*, 1978.

[21] D E Siegfried and P J Wilbur. Studies on an experimental quartz tube hollow cathode. *14th International Electric Propulsion Conference*, 1979. AIAA-1979-2056.

[22] M. Krishnan, R. G. Jahn, W. F. von Jaskowsky, and K. E. Clark. Physical processes in hollow cathode discharge. *AIAA Journal*, 15(9):1217–1223, 1977.

[23] D Pedrini, F Cannelli, C Ducci, T Misuri, F Paganucci, and M Andrenucci. Hollow Cathodes Development at SITAEL. *Space Propulsion*, 2016.

[24] Riccardo Albertoni. *Cathode Processes in MPD Thrusters*. Ph. d., Universita Degli Studi di Pisa, 2012.

[25] Abdelhakim Salhi. *Theoretical and experimental studies of orificed, hollow cathode operation*. Ph.d., The Ohio State University, 1993.

[26] Rohit Shastry, Daniel Herman, George Soulas, and Michael Patterson. Status of nasa's evolutionary xenon thruster (next) long-duration test as of 50,000 h and 900 kg throughput. In *33rd International Electric Propulsion*

Conference, 2013. IEPC-2013-121.

[27] D.M. Goebel and I. Katz. *Fundamentals of Electric Propulsion: Ion and Hall Thrusters*. John Wiley & Sons, Inc., 2008.

[28] D. M. Goebel and E. Chu. High-current lanthanum hexaboride hollow cathode for high-power hall thrusters. *Journal of Propulsion and Power*, 30(1):35–40, 2014.

[29] D. M. Goebel and E. Chu. High current lanthanum hexaboride hollow cathodes for high power hall thrusters. In *32nd International Electric Propulsion Conference*, 2011. IEPC-2011-053.

[30] Daniel L. Brown, Brian E. Beal, and James M. Haas. Air Force Research Laboratory High Power Electric Propulsion Technology Development. In *IEEE Aerospace Conference*, 2009.

[31] Richard R Hofer, Thomas M Randolph, David Y Oh, John Steven Snyder, and Kristi H de Grys. Evaluation of a 4.5 kw commercial hall thruster system for nasa science missions. In *42nd AIAA/ASME/SAE/ASEE Joint Propulsion Conference & Exhibit*, 2006. AIAA-2006-4469.

[32] Matthew Plasek, Christopher J. Wordingham, Sebastián Rojas Mata, Nicholas Luzarraga, and Edgar Y. Choueiri. Experimental investigation of a large-diameter cathode. In *50th AIAA/ASME/SAE/ASEE Joint Propulsion Conference & Exhibit*, 2014. AIAA-2014-3825.

[33] Pierre-Yves C. R. Taunay. *Scaling Laws in Orificed Thermionic Hollow Cathodes*. Ph.d., Princeton University, 2020.

[34] I Katz, I G Mikellides, D M Goebel, and J E Polk. Insert heating and ignition in inert-gas hollow cathodes. *IEEE Transactions on Plasma Science*, 36(5):2199–2206, 2008.

[35] Riccardo Albertoni, Daniela Pedrini, Fabrizio Paganucci, and Mariano Andrenucci. A Reduced-Order Model for Thermionic Hollow Cathodes. *IEEE Transactions on Plasma Science*, 41(7):1731–1745, 2013.

[36] A. Lorente-Arcas. A Model for the Hollow Cathode Discharge. *Plasma Physics*, 14:651–659, 1972.

[37] Daniel E Siegfried. *A Phenomenological Model for Orificed Hollow Cathodes*. Ph.d., Colorado State University, 1982.

[38] Christopher J. Wordingham, Pierre-Yves C. R. Taunay, and Edgar Y. Choueiri. A critical review of orificed hollow cathode modeling: 0-d models. In *53rd AIAA/ASME/SAE/ASEE Joint Propulsion Conference*, 2017. AIAA-2017-4888.

[39] Ira Katz, John R Anderson, James E Polk, and John R Brophy. One-Dimensional Hollow Cathode Model. *Journal of Propulsion and Power*, 19(4):595–600, 2003.

[40] Ioannis G. Mikellides, Ira Katz, Dan M. Goebel, and James E. Polk. Hollow cathode theory and experiment. II. A two-dimensional theoretical model of the emitter region. *Journal of Applied Physics*, 98(11):113303, 2005.

[41] Shuai Cao, Junxue Ren, Haibin Tang, Ruojian Pan, Zhe Zhang, Kaiyu Zhang, and Jinbin Cao. Modeling on plasma energy balance and transfer in a hollow cathode. *Journal of Physics D: Applied Physics*, 52(28):285202, 2019.

[42] Kenichi Kubota, Yuya Oshio, Hiroki Watanabe, Shinatora Cho, Yasushi Ohkawa, and Ikkoh Funaki. Hybrid-pic simulation of lab6 hollow cathode self-heating characteristics. *TRANSACTIONS OF THE JAPAN SOCIETY FOR AERONAUTICAL AND SPACE SCIENCES*, 62(1):11–19, 2019.

[43] Gaétan Sary, Laurent Garrigues, and Jean-Pierre Boeuf. Hollow cathode modeling: I. a coupled plasma thermal two-dimensional model. *Plasma Sources Science and Technology*, 26(5):055007, 2017.

[44] Gaétan Sary, Laurent Garrigues, and Jean-Pierre Boeuf. Hollow cathode modeling: Ii. physical analysis and parametric study. *Plasma Sources Science and Technology*, 26(5):055008, 2017.

[45] Pablo Guerrero, Ioannis G. Mikellides, James E. Polk, and Daniel I. Meiron. Hollow cathode thermal modelling and self-consistent plasma solution: work function evaluation for a lab_6 cathode. *AIAA Propulsion and Energy Forum*, 2018. AIAA-2018-4511.

[46] Pablo Guerrero, Ioannis G. Mikellides, James E. Polk, Rosa Carmina Monreal, and Daniel I. Meiron. Hollow cathode thermal modelling and self-consistent plasma solution two step neutralization modelling. *36th International Electric Propulsion Conference*, 2019. IEPC-2019-A-301.

[47] Edmund K. Storms. The emissivity of LaB6 at 650 nm. *Journal of Applied Physics*, 50(6):4450, 1979.

[48] Jeremy M.D. Kowalczyk, Michael R. Hadmack, Eric B. Szarmes, and John M.J. Madey. Emissivity of lanthanum hexaboride thermionic electron gun cathode. *International Journal of Thermophysics*, 35(8):1538–1544, 2014.

[49] Ioannis G. Mikellides, Ira Katz, Dan M. Goebel, James E. Polk, and Kristina K. Jameson. Plasma processes inside dispenser hollow cathodes. *Physics of Plasmas*, 13:063504, 2006.

[50] Ioannis G Mikellides, Alejandro Lopez Ortega, Dan M Goebel, and Giulia Becatti. Dynamics of a hollow cathode discharge in the frequency range of 1–500 khz. *Plasma Sources Science and Technology*, 29(3):035003, 2020.

[51] J. Scott Miller, Steve H. Pullins, Dale J. Levandier, Yu Hui Chiu, and Rainer A. Dressler. Xenon charge exchange cross sections for electrostatic thruster models. *Journal of Applied Physics*, 91(3):984–991, 2002.

[52] Michael Hause, Benjamin Prince, and Raymond Bemish. Krypton charge exchange cross section for Hall effect thruster models. *Journal of Applied Physics*, 113(16):163301, 2013.

[53] Mitchner M. and Charles H Kruger. *Partially Ionized Gases*. 1973. p. 153.

[54] Michael A. Lieberman and Allan J. Lichtenberg. *Principles of Plasma Discharges and Materials Processing*. Wiley Interscience, 2005. p. 136.

[55] G. D. Hobbs and J. A. Wesson. Heat flow through a Langmuir sheath in the presence of electron emission. *Plasma Physics*, 9(1):85–87, 1967.

[56] PD Prewett and JE Allen. The double sheath associated with a hot cathode. In *Proceedings of the Royal Society of London A: Mathematical, Physical and Engineering Sciences*, volume 348, pages 435–446. The Royal Society, 1976.

[57] Ioannis G Mikellides. Effects of viscosity in a partially ionized channel flow with thermionic emission. *Physics of Plasmas*, 16(1):013501, 2009.

[58] M J Mandell and I Katz. Theory of hollow cathode operation in spot and plume modes. 1994. AIAA-1994-3134.

[59] Matthew Thomas Domonkos. *Evaluation of low-current orificed hollow cathodes*. Ph.d., University of Michigan, 1999.

[60] Christopher J. Wordingham, Pierre-Yves C. R. Taunay, and Edgar Y. Choueiri. Theoretical prediction of the dense-plasma attachment length in an orificed hollow cathode. In *35th International Electric Propulsion Conference*, 2017. IEPC-2017-566.

[61] Makoto Hayashi. Bibliography of electron and photon cross sections with atoms and molecules published in the 20th century - xenon. Technical Report NIFS-DATA-79, NIFS, 2003.

[62] Eric Jones, Travis Oliphant, Pearu Peterson, et al. SciPy: Open source scientific tools for Python, 2001–. Online.

[63] Ira Katz, John Anderson, James Polk, and John Brophy. A Model of Hollow Cathode Plasma Chemistry. *38th AIAA/ASME/SAE/ASEE Joint Propulsion Conference & Exhibit*, 2002. AIAA-2002-4241.

[64] Ira Katz, James E Polk, Ioannis G Mikellides, Dan M Goebel, and Sarah E Hornbeck. Combined plasma and thermal hollow cathode insert model. In *29th International Electric Propulsion Conference*, 2005. IEPC-2005-228.

[65] Giulia Becatti, Dan M. Goebel, James E. Polk, and Pablo Guerrero. Life evaluation of a lanthanum hexaboride hollow cathode for high-power hall thruster. *Journal of Propulsion and Power*, 34(4):893–900, 2018.

[66] Pierre-Yves Taunay, Christopher J Wordingham, and Edgar Y Choueiri. Open electric propulsion with an application to thermionic orificed hollow cathodes. *AIAA Propulsion and Energy Forum*, 2020. AIAA-2020-3638.

[67] Pierre-Yves C. R. Taunay and Edgar Y. Choueiri. Multi-wavelength pyrometry based on robust statistics and cross-validation of emissivity model. *Review of Scientific Instruments*, 91(11), 2020.

[68] Gareth James, Daniela Witten, Trevor Hastie, and Robert Tibshirani. *An Introduction to Statistical Learning*. Springer, 2013. p.66.

[69] Pierre-Yves C. R. Taunay, Christopher J. Wordingham, and Edgar Y. Choueiri. The influence of ambipolar diffusion on the attachment length and electron temperature in orificed hollow cathodes. In *36th International Electric Propulsion Conference*, 2019. IEPC-2019-A628.

[70] Dan M Goebel, Kristina K Jameson, and Richard R Hofer. Hall thruster cathode flow impact on coupling voltage and cathode life. *Journal of Propulsion and Power*, 28(2):355–363, 2012.